Heliyon 10 (2024) e37808

Contents lists available at ScienceDirect

Heliyon

journal homepage: www.cell.com/heliyon

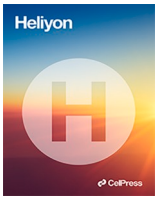

Research article

Fast fabrication of superhydrophobic Ti-6Al-4V surface using Q-switched nanosecond pulsed laser at 1064 nm and cyclohexane

Muhammad Budi Haryono, Kaung Wai Yan Lin, Tanant Waritanant *

School of Materials Science and Innovation, Faculty of Science, Mahidol University, Thailand

ARTICLE INFO

Keywords:
Nanosecond laser
Ti-6Al-4V
Laser-textured surface
Cyclohexane
Superhydrophobic surface

ABSTRACT

Superhydrophobic and superhydrophilic surfaces are attracting significant attention in fundamental and applied research. This study fabricated the micro/nanostructure with a Q-switched nanosecond pulsed laser on the Ti-6Al-4V surface. Three laser-generated surface topographies on titanium were produced based on three different pitch sizes (51 μm, 34 μm, and 29 μm). The laser textured surfaces (LTS) were studied in terms of both structure evolution and chemical composition using Field Emission Scanning Electron Microscopy (FE-SEM), Optical Microscopy (OM), Confocal Laser Scanning Microscopy (CLSM), Raman Spectroscopy, and X-ray Diffractometer (XRD). 29 μm pitch displayed the lowest water contact angle of 18.5° and surface roughness of 0.5 μm. This structure was further treated with cyclohexane at different temperatures. The best sample reached superhydrophobicity with a maximum water contact angle of 155.1° immediately after being treated with cyclohexane at the low temperature of 70 °C for 2 h, while the raw surface, for comparison, showed no change in hydrophobicity after being treated with cyclohexane under the same condition. Thus showing clear evidence of a combined effect between LTS and post-treatment. The surface features were assessed to explain the underlying process.

1. Introduction

Titanium alloys, specifically Ti-6Al-4V, are currently one of the most desirable metals for medical devices. Ti-6Al-4V is used in implant devices, such as prosthetic hips and knees, bone plates, artificial hearts, pacemakers, connectors for fracture fixation, and cardiac valve prostheses [1]. However, in practice, pathogenic microbes, including Staphylococcus aureus, Escherichia coli, and Pseudomonas aeruginosa, can potentially attach to these medical devices. This attachment can lead to severe infections and potentially fatal outcomes, as well as increased healthcare expenditures [2]. In recent years, surface topography manipulation has played a larger role in controlling microbial and cellular attachment on different material surfaces. For instance, the generation of micro- or nanoscale features on the surfaces can enhance antibacterial properties by preventing bacterial adhesion and/or killing/inactivating adherent bacteria altogether [3]. On the other hand, certain micro/nanoscale surface features can enhance cellular development and proliferation [4]. Gotfredsen et al. [5] compared the surface characteristics of titanium implants to induce a bone reaction. The results indicated that plasma-sprayed titanium manifested more significant surface irregularity than machined titanium. Grizon et al. [6] also studied the effect of varied surface roughness on Ti implants, showing that the bone reaction was higher on the coarser surface than on the smooth surface.

Similarly, various studies have investigated the relationship between surface hydrophobicity and bacterial attachment. Some have

* Corresponding author. School of Materials Science and Innovation, Mahidol University, Thailand.
E-mail address: tanant.war@mahidol.ac.th (T. Waritanant).

https://doi.org/10.1016/j.heliyon.2024.e37808
Received 30 April 2024; Received in revised form 27 August 2024; Accepted 10 September 2024
Available online 11 September 2024

reported that the number of adhered bacteria decreases significantly as the surface hydrophobicity increases, and bacteria affixed to hydrophobic materials are also more easily removed by an air-bubble jet or increased flow [7–9]. Looking beyond simple hydrophobicity, superhydrophobic surfaces, which mimic shark skins and lotus leaves in nature, have shown high potential as tools to prevent the attachment of microorganisms [10–12]. Additionally, there has been a significant increase in interest in the various special characteristics of superhydrophobic surfaces, such as self-cleaning, corrosion protection, and anti-icing [13]. There are three main approaches to creating superhydrophobic surfaces. The first approach is to physically change the surface roughness [14], the second approach involves altering the chemical composition of the surface to reduce the surface energy, and the third approach utilizes both physical and chemical alterations [15].

Many studies have used laser processing to generate hierarchical structures at the micro and nanoscale [16]. This technique has successfully utilized various laser sources, encompassing a diverse array of wavelength, pulse duration, energy, and frequency combinations [17]. The implementation of nanosecond laser machining has demonstrated its potential as a promising and economically viable approach for surface texturing to obtain hydrophilic and/superhydrophobic metal structures, in contrast to femtosecond or picosecond lasers, which are much more cost-prohibitive [18,19]. The application of nanosecond laser technology has even become increasingly common in the production of surface, precise micro and nanostructures, such as nanopillars and microgrooves independent from substrates [20], that exhibit strong hydrophobic properties and durable micro-roughness [14,21,22].

However, the hydrophilicity of laser-textured surface (LTS) on Ti-6Al-4V cannot change to a superhydrophobic level immediately after laser processing as demonstrated by D. Huerta-Murillo et al. [23] where the fabricated multi-scale periodic surface textures on Ti-6Al-4V has the water contact angle increased from 67 ± 2° on the raw surface to 91 ± 3° on LTS. Deepak Patil et al. [24] also fabricated a pit structure on Ti-6Al-4V by a nanosecond laser (Nd: YAG) and the results showed the hydrophobicity increased from 63° water contact angle on the raw surface to approximately 140° after a natural aging period in ambient environment of 20 days. To overcome this limit, LTS in combination with other treatments is required to produce superhydrophobic surfaces within a short time window.

Fast fabrication of superhydrophobic titanium surfaces can be achieved by first roughening the surface and then covering it with chemical compounds that have low surface energy [29–32]. Normally, a wide range of silane coupling agents were employed by the majority of researchers [33,34], stearic acid, flurosilane [35], polysilazane [18], and perhydropolysilazane (PHPS) [15] as low surface free energy modifiers. However, these low surface energy modifiers have certain shortcomings, such as being expensive, toxic, and unstable, limiting their real-life application. Rajab et al. [29] produced a superhydrophobic surface (150.48°–160°) on Ti-6Al-4V by combining macro/micro/nanostructure produced by picosecond laser and then soaked the LTS into fluoroalkysilane (FAS) for 2 h. Yuxin Wang et al. [28] produced a superhydrophobic surface on TC4 alloy by treated LTS with anodizing and FAS-assisted low-temperature annealing of 150 °C for 20 min. Zheng et al. [32] fabricated a superhydrophobic surface using a picosecond laser and treated it with chemical fluorination. As shown in Table 1, many researchers use nanosecond lasers at 1064 nm and chemical modifiers to produce a superhydrophobic Ti-6Al-4V surface.

Motivated by the earlier ideas, this study generated LTS on Ti-6Al-4V by Q-switched nanosecond laser. The high wall-plug efficiency of the Nd:YAG nanosecond pulse laser operating at the chosen wavelength of 1064 nm, its fundamental wavelength, also makes it suitable for various uses, including large-scale production [36].

After laser texturing, this work used cyclohexane as an alternative chemical modifier to produce a superhydrophobic Ti-6Al-4V surface. Cyclohexane (C_6H_{12}) as a chemical modifier is a solute exhibiting hydrophobic properties [37]. Hydrophobicity or superhydrophobicity can be achieved by employing cyclohexane as a coating layer. However, the information is still limited. Ying Ma et al. [38] produced a superhydrophobic surface on PMMA with cyclohexane-assisted low-temperature annealing at 70 °C for 20 min. The water contact angle (CA) of raw PMMA was 67.8 ± 1.4°. The water contact angle increased to 164.3 ± 3.9° on the raw surface after

Table 1
Summary of laser-textured surfaces on titanium using nanosecond laser at 1064 nm.

Materials	Year (ref)	Original WCA (°)	Patterns	Post-processing (Chemical modifiers or additional treatments)	Processing duration (h)	Max WCA (°)
Pure Ti	2016 [25]	77.8	Line	–	720 h	157.2
Ti-6Al-4V	2017 [23]	67 ± 2	μ-cell	–	No information	91.3
Ti-6Al-4V	2018 [24]	63	Pit	Annealing at the temperature of 300 °C in a microprocessor-based-temperature controlled furnace	2 h	162
Ti-6Al-4V	2018 [18]	–	Micro/nanoscale hierarchical structure	Organic polysilazane, KH570, isopropanol, and nano-sized zinc oxide particles	7 h 40 min	164.1 (1 h) 157 (>1 h)
Ti-6Al-4V	2020 [26]	77	Grid	Surface texturing in ethanol and then low annealing at a temperature of 150 °C	4 h (Annealing Process)	154.9
Ti-6Al-4V	2022 [27]	62	Nanoporous	1H,1H,2H,2H-Perfluor ooctyltriethoxysilane-ethanol solution	1 h	137
Ti-6Al-4V	2022 [28]	72	Grid	Anodizing, Fluorosilane, 1H, 1H, 2H, 2H-Perfluorodecyltrimethoxysilan, H_3PO_4, $H_2C_2O_4$, and NaF	1 h	158
Ti-6Al-4V	2024 (This work)	100.3 ± 9.5	Micro/nanoscale hierarchical structure	Cyclohexane- assisted low temperature annealing of 70 °C	2 h	155.1

being treated with warm cyclohexane. Lu Gong et al. [39] used cyclohexane to increase silicon substrate hydrophobicity via surface-initiated emulsion polymerization. The water contact angle on the silicon substrate increased from 80.9° to 123.7°. Cyclohexane exhibits a comparatively low level of toxicity and does not elicit detrimental effects on the bloodstream, unlike benzene [40]. Cyclohexane has a melting temperature of 6.47 °C and a boiling temperature of 80.7 °C and is already predominantly encountered by the general populace via ambient air intake, owing to its widespread occurrence in gasoline vapors, volcanic emissions, plant volatiles, and cigarette smoke. The urinary system divides and eliminates a small fraction of the substance. The metabolites of cyclohexane undergo conjugation, predominantly with glucuronides and potentially with sulfates, and are subsequently eliminated through urinary excretion [41,42]. This work applied three different pitch sizes to fabricate LTS on Ti-6Al-4V surfaces. The most hydrophilic sample was chosen as a sample treated with cyclohexane at various temperatures. This technique can immediately produce a superhydrophobic Ti-6Al-4V surface in the following sections by subjecting LTS to a low cyclohexane temperature. This strategy offers the possibility of a future technique for generating superhydrophobic Ti-6Al-4V surfaces.

2. Materials and methods

2.1. Materials and laser processing preparations

The Ti-6Al-4V sheet with a thickness of 0.5 mm was ordered from Jianghehai and Steel Group Co., Ltd. The chemical compositions (wt%) of Ti-6Al-4V as shown in Table 2 was obtained from the quality certificate provided by Jianghehai and Steel Group Co., Ltd. The Ti-6Al-4V sheet was cut into dimensions of 3 mm x 3 mm. These plates were conditioned by mechanical polishing to an initial surface roughness (S_a) of 0.28 μm and S_z at 3.88 ± 0.12 μm. Subsequently, the samples were ultrasonically cleaned in ethanol for 30 min and later in deionized water for 30 min. After washing, the samples were dried by blowing air over the samples.

The laser used was a Nd:YAG 1064-nm infrared nanoseconds pulsed laser, manufactured by Changchun New Industries Optoelectronics Tech. CO., Ltd, China. The polished samples were ablated using a Q-switched Nd:YAG laser 1064 nm with specific parameters, as shown in Table 3. The laser had a focusing lens with a diameter of 25.4 mm and operated at a repetition rate of 10 Hz. Each pulse had an energy of 4.7 mJ and a duration of 10.7 ns.

The laser beam was focused to a spot diameter of 56 μm in air without assist gas. The distance between the laser and the sample measured 262 cm. The scanning was performed using the parallel line regime. The different pitch sizes were used as laser processing parameters to fabricate LTS on Ti-6Al-4V surfaces. The samples labeled "P29" were processed using laser parameters of 29 μm pitch size while a pitch size of 34 μm was used for the samples labeled "P34" and a pitch size of 51 μm was used in the case of the samples labeled "P51". Fig. 1(a) illustrates a schematic image of the nanosecond pulsed laser system. The laser setup used two output couplers (OC) and five folding mirrors (M). The scanning was conducted using computer-controlled XYZ equipment. THORLABS offers a stage equipped with a piezo inertia drive. The laser beam was directed towards the titanium alloy sheets on the production system. Fig. 1(b) depicts a schematic image of the scanning design.

2.2. Post-processing

Following laser processing, P29 samples were not subjected to any cleaning treatment before post-processing. P29 samples were immediately soaked in 20 mL of cyclohexane in a glass beaker. The samples were then heated on a hot plate for 2 h at various temperatures of cyclohexane under normal environmental conditions. "P29"-labeled for P29 without cyclohexane treatment. The P29 samples were labeled as "P29-C70" for P29 treated with cyclohexane at a temperature of 70 °C. P29 was subjected to cyclohexane at a temperature of 300 °C and afterward labeled as "P29-C300". After that, P29-C70 and P29-C300 were subsequently dried at room temperature for 12 h.

2.3. Surface characterization

The surface morphology and surface composition of the laser-textured surface were analyzed using Field Emission Scanning Electron Microscopy (FE-SEM), Optical Microscopy (OM), Confocal Laser Scanning Microscopy (CLSM), Raman Spectroscopy, and X-ray Diffractometer (XRD). An accelerating voltage of 10 kV was utilized for the HITACHI SU8010 FE-SEM. Motic OM was used to analyze the microstructure of the samples. LEXT CLSM from OLYMPUS determines the substratum macro and micro surfaces. The LEXT analyzer software was used for measure control and data analysis. A Raman spectroscopic analysis was conducted using a Horiba Raman Microscope equipped with a 532 nm laser. The samples underwent analysis using the 50× objective with a duration of exposure of 10 s, and a total of 10 accumulations were captured. In this experiment, phase composition and crystalline size were analyzed using Bruker D2 phaser XRD under the following conditions: a time/step ratio of 0.8, 3001 steps, and 2508 s.

The sessile drop technique measured the wettability on the sample's surface. Deionized (DI) water with a droplet volume of

Table 2
Chemical compositions (wt%) of Ti-6Al-4V.

Element	Ti	Al	V	Fe	O	C	N	H	Y
Composition in wt(%)	89	6.18	4.25	0.3	0.2	0.08	0.05	0.015	0.005

Table 3
Parameters of laser processing for samples studied in this work.

Parameters	P29	P34	P51
Energy (mJ/pulse)	4.7	4.7	4.7
Scanning Speed (cms^{-1})	0.015	0.016	0.041
Repetition Rate (Hz)	10	10	10
Pitch (μm)	29	34	51

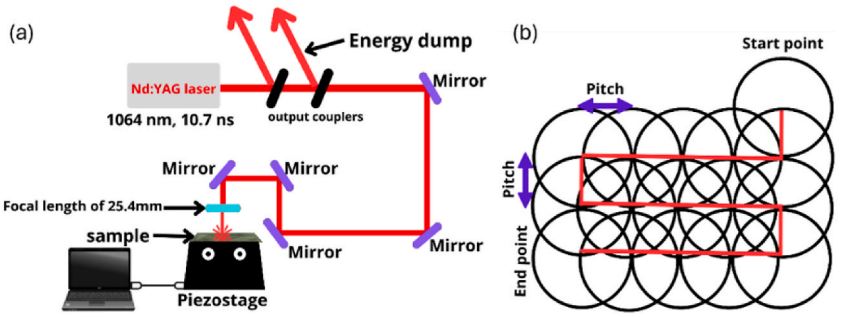

Fig. 1. Schematic diagram of (a) nanosecond pulsed laser system and (b) scanning directions.

approximately 4 μl was used in this technique. A syringe was used to inject DI water onto the sample surface, followed by capturing a picture using a SANYO VCC-5755P camera. The contact angle of the water droplet was measured three times to obtain an average value. The contact angle was calculated by examining the droplet image via ImageJ software.

3. Results and discussions

3.1. Analysis of laser-textured Ti-6Al-4V surfaces

3.1.1. Single laser spot analysis

The confocal laser scanning microscopy (CLSM) images and the corresponding profile are shown in Fig. 2. The average diameter and total height of the ablation spots, measured from the top layer to the valley bottom, are 53.3 ± 4.5 μm and 9.6 ± 2.3 μm, respectively. It was observed that the ablation spot diameter was smaller than the design diameter of 56 μm. Nanosecond laser texturing results in a microscale recast layer after ablation, as shown in Fig. 2(c). This microscale recast layer is produced from resolidified metal molten and redeposition of nanoparticles along the edge.

3.1.2. Effects of laser parameters on surface morphology

Fig. 3 shows images of Ti-6Al-4V surfaces before and after laser texturing. The initial Ti-raw surface shows scratches from the mechanical polishing process, which are eliminated following laser texturing, resulting in distinct surface topography. Diverse surface textures on the Ti-6Al-4V surface after laser texturing are created by reducing pitch size and scanning speed from a pitch size of 51 μm with a scanning speed of 0.041 cms^{-1} to a pitch size of 29 μm with a scanning speed of 0.015 cms^{-1}. The valley width (V_w) on LTS decreased from 29.5 ± 4 μm at P51 to 20.9 ± 3 μm at P34 and 18 ± 2.3 μm at P29, as shown in Fig. 3(j). The total height (S_z) increased from 4.4 ± 0.2 μm (P51) to 5.5 ± 0.4 μm (P34) and 6.4 ± 0.3 μm (P29), as seen in Fig. 3(j). The surface roughness (S_a) rose from 0.3 ± 0.02 μm at P51 to 0.47 ± 0.02 μm at P34 and 0.5 ± 0.01 μm at P29, as illustrated in Fig. 3(k). The observed increase in surface roughness is related to the geometry changes induced by laser texturing. FE-SEM images confirm that surface morphology became rougher with pitch size reduction to 29 μm, as shown in Fig. 4.

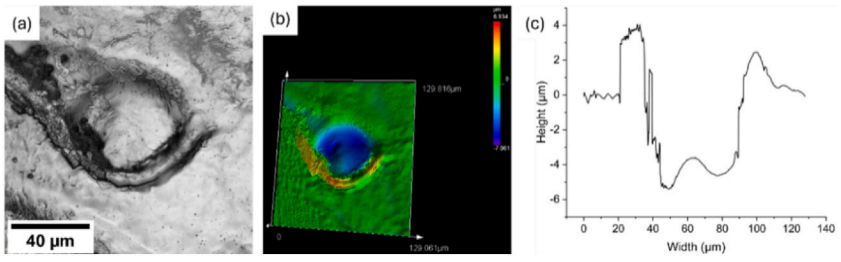

Fig. 2. Confocal laser scanning microscopy (CLSM) images of a single ablation spot: (a) 2D images, (b) 3D images, and (c) surface profile.

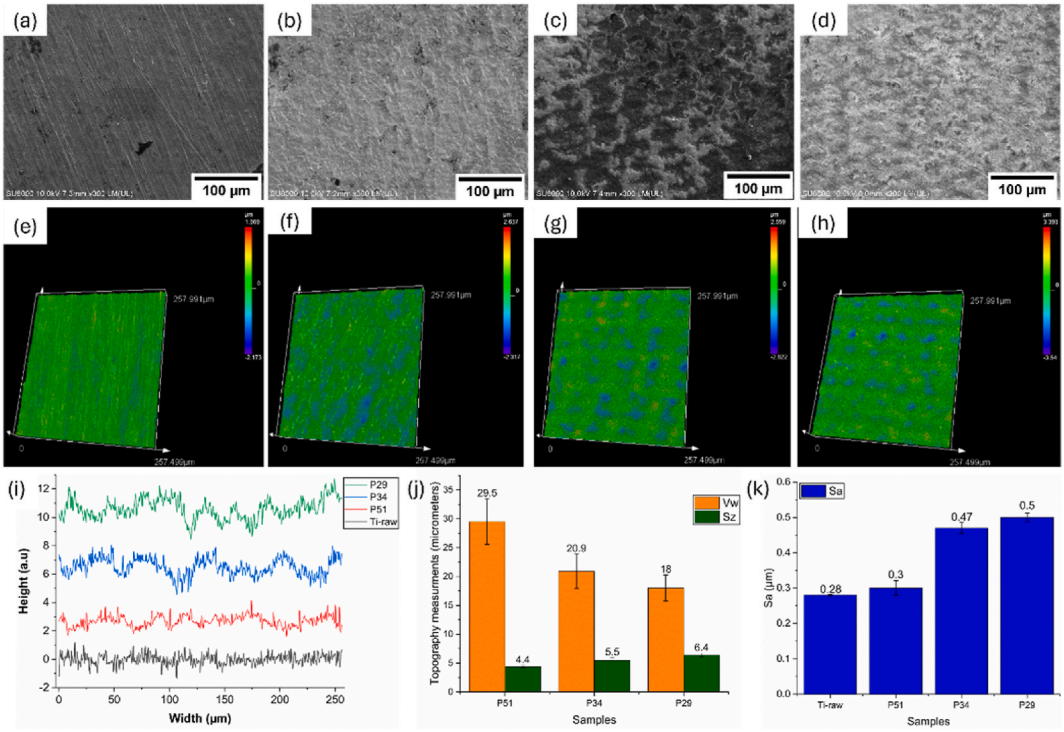

Fig. 3. Surface topography observed under FE-SEM and CLSM for different LTS (a, e) Ti-raw, (b, f) P51, (c, g) P34, (d, h) P29, (i) presents the surface profile from different LTS, (j) compares the valley width (V_w) and height (S_z) across the LTS samples, (k) surface roughness (S_a) for different LTS.

3.1.3. Chemical composition of laser-textured surface

Figs. 5 and 6 demonstrate the impact of laser processing on the composition and phase of Ti-6Al-4V. The Raman spectra of P51 exhibit rutile peaks at 241 cm^{-1}, 427 cm^{-1}, and 610 cm^{-1}. In contrast, the Raman spectra of P34 demonstrate three different types of TiO_2: anatase (A) at 144 cm^{-1}, rutile (R) at 271 cm^{-1} and 603 cm^{-1}, and brookite (B) at 403 cm^{-1}. The Raman spectra of P29 display anatase peaks at 145 cm^{-1} and rutile peaks at 241 cm^{-1}, 422 cm^{-1}, and 605 cm^{-1}. Among these, the peak intensity of TiO_2 is lowest in P51 when compared to P34 and P29.

Fig. 6 shows the X-ray diffraction (XRD) phase analysis of the Ti-raw and LTS surfaces. All samples predominantly exhibit α-Ti in the XRD patterns, corresponding to the JCPDS 00-001-1198 standard. The observed peaks are arranged in a left-to-right sequence corresponding to crystals with atomic planes (100), (002), (101), (102), (103), and (112). In all LTS samples, anatase (004) is observed at varying peak intensities. Nevertheless, the rutile (210) phase is observed exclusively in P34 and P29, with these TiO_2 phases corresponding to JCPDS 75–1537.

3.1.4. Surface color

The color of the LTS observed through optical microscopy (OM) varies depending on the laser parameters applied to the Ti-6Al-4V surfaces. The LTS shows noticeable color differences between the P29, P34, and P51 surfaces, as seen in Fig. 7. The OM images reveal that P29 and P34 appear darker than P51, which corresponds with Raman spectra and XRD results, indicating the presence of rutile phases in P29 and P34.

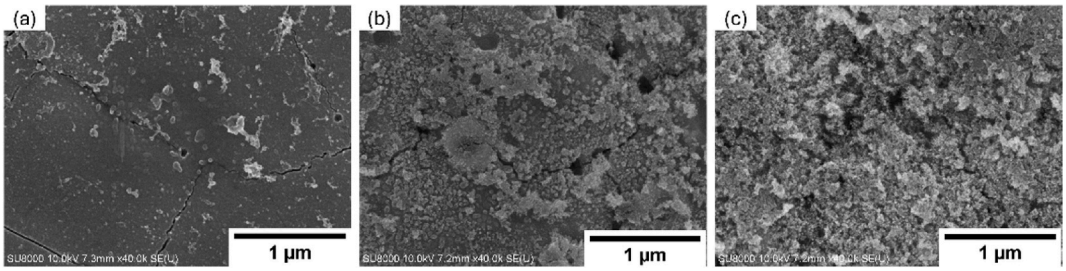

Fig. 4. Different LTS morphology under FE-SEM at a high magnification of 40.0k: (a) P51, (b) P34, and (c) P29.

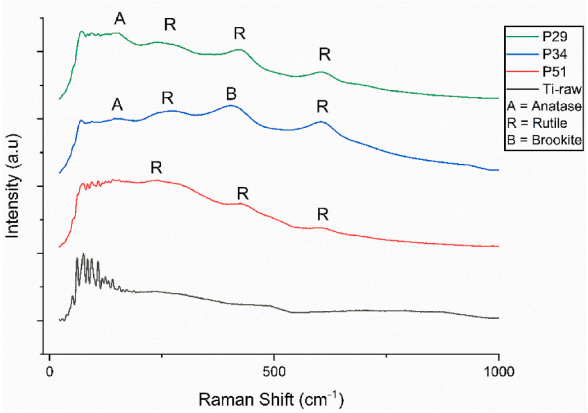

Fig. 5. Raman spectroscopy results of different Ti-6Al-4V surfaces. A represents anatase, R is rutile, and B represents brookite.

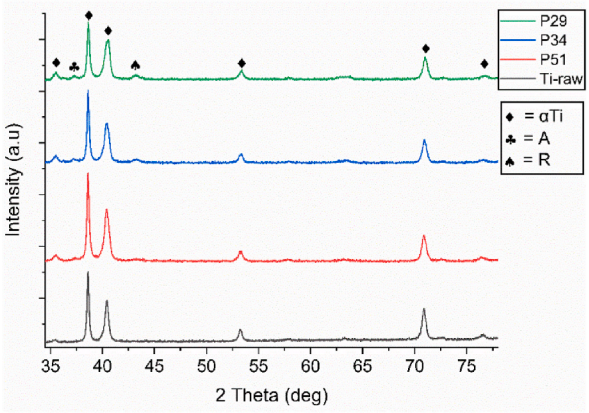

Fig. 6. XRD patterns of differences Ti-6Al-4V surfaces. A represents anatase, and R is rutile.

3.1.5. Wettability

Surface texturing by laser processing significantly altered the hydrophobicity of the Ti-6Al-4V surface, resulting in increased hydrophilicity. This transformation is illustrated in Figs. 8 and 9. Hydrophilicity increased significantly from a water contact angle of 100.3 ± 9.5° on the Ti-raw to a water contact angle of 43.9 ± 9.6° on the P51 surface. Hydrophilicity further increased with a reduction in pitch size, with a water contact angle of 22.3 ± 2.4° at 34 μm and 18.5 ± 5.2° at 29 μm.

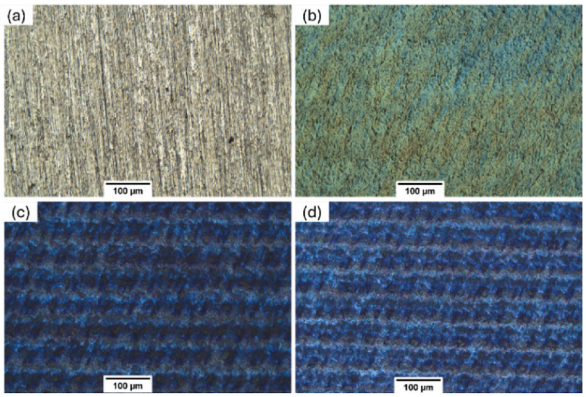

Fig. 7. The color surfaces on LTS under optical microscopy: (a) Ti-raw, (b) P51, (c) P34, and (d) P29.

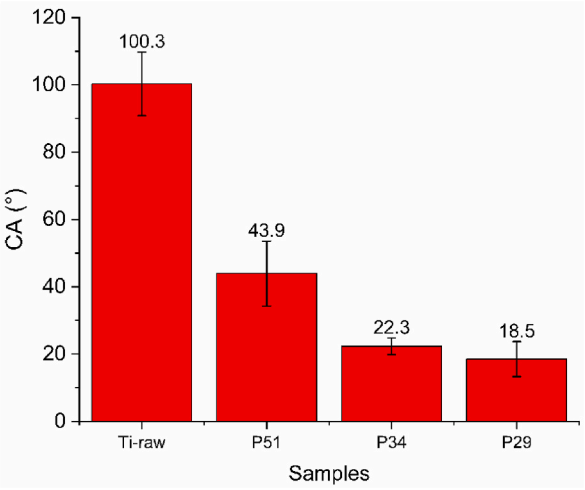

Fig. 8. The wettability transition after laser processing.

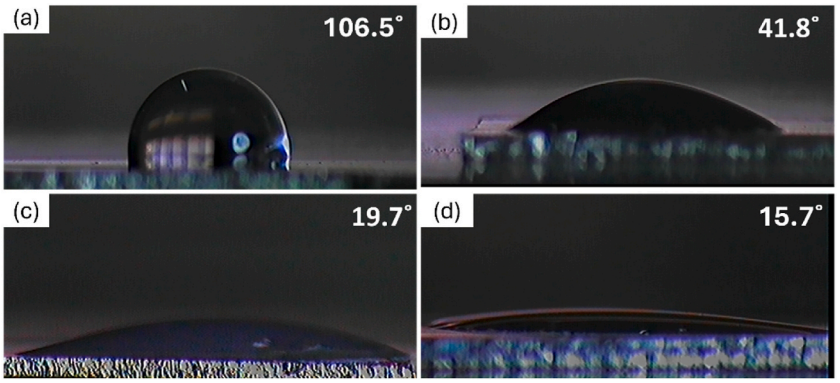

Fig. 9. The water droplet images on different LTS are taken by SANYO VCC-5755P camera: (a) Ti-raw, (b) P51, (c) P34, (d) P29.

3.2. *Effects of post-processing*

3.2.1. *Surface morphology and topography*

The surface roughness was characterized using several parameters: S_q represents the root mean square height; the root means square gradient by S_{dq}, and the developed interfacial area ratio by S_{dr}. Surface roughness (S_a) increased from 0.28 ± 0.00231 μm to 0.5 ± 0.01 μm after surface texturing, as shown in Fig. 10(a). However, S_a decreased to 0.39 ± 0.003 μm on P29-C70 and 0.44 ± 0.02 μm on P29-C300. Fig. 10(a) shows that the S_q values have a similar trend to S_a. S_q increased from 0.36 ± 0.005 μm (Ti-raw) to 0.62 ± 0.02

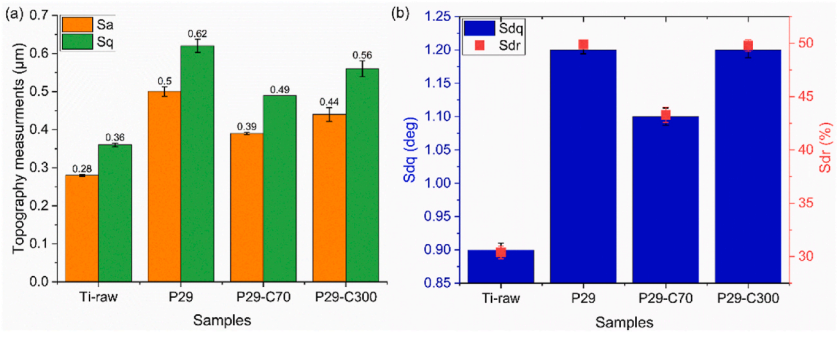

Fig. 10. S-values obtained using CLSM for LTS before and after treatment with cyclohexane (a) surface topography measurements on different Ti-6Al-4V topographies, and (b) S_{dq} and S_{dr} results on different Ti-6Al-4V topographies.

μm (P29) after surface texturing and decreased to 0.49 ± 0 μm (P29-C70) and 0.56 ± 0.02 μm (P29-C300). S_{dq} and S_{dr} values also follow the trends of S_a and S_q, as shown in Fig. 10(b). S_{dq} increased from 0.9 ± 0.01° to 1.2 ± 0.01° after laser texturing, while S_{dr} rose from 30.4 ± 0.6 % to 49.9 ± 0.4 %. After P29 was treated with low-temperature cyclohexane at 70 °C, S_{dq} and S_{dr} decreased to 1.1 ± 0.01° and 43.3 ± 0.7 %, respectively. When the P29 was treated with cyclohexane at 300 °C, S_{dq} and S_{dr} values remained similar to those of untreated P29, with S_{dq} of 1.2 ± 0.01° and S_{dr} of 49.8 ± 0.55 %.

S_a, S_q, S_{dr}, and S_{dq} decreased due to cyclohexane treatment on the LTS. P29-C70 exhibited lower S_a, S_q, S_{dr}, and S_{dq}, indicating a smoother surface compared to P29 and P29-C300, as shown in Fig. 11. However, when the P29 was treated with high-temperature cyclohexane at 300 °C, the surface exhibited increased roughness compared to P29-C70, with a bigger nanoparticle observed than those present on untreated P29. These results indicate that the post-processing temperature significantly influences the interaction between cyclohexane and P29, affecting surface roughness.

3.2.2. Raman spectroscopy

Analysis of the Raman spectra identified four different surface topographies, as shown in Fig. 12. The Raman spectra revealed the presence of anatase and rutile on LTS samples, both with and without cyclohexane treatment. The Raman peaks corresponding to anatase (156 cm^{-1}) and rutile (241 cm^{-1}, 422 $cm^{-1,}$ and 605 cm^{-1}) were observed in P29 samples, including those subjected to surface texturing by laser. Following cyclohexane-assisted low-temperature annealing of 70 °C (P29-C70), the peaks for anatase and rutile (605 cm^{-1}). However, anatase and rutile (605 cm^{-1}) peaks were less distinct on the P29-C300 surface.

3.2.3. Surface color

Treatment of P29 with cyclohexane at different temperatures led to noticeable changes in surface color, as shown in Fig. 13. The untreated P29 showed a predominantly dark color. In comparison, P29-C70 developed red, while P29-C300 surfaces showed a bright color.

3.2.4. Wettability

The P29 sample exhibited the lowest CA at 18.5 ± 5.2° in this study. This untreated P29 was labeled as "P29". After P29 was treated with cyclohexane at 70 °C resulted in a significant increase in CA to 151.1 ± 3.6°, categorizing it as "P29-C70", as shown in Figs. 14 and 15. In contrast, when P29 was treated with cyclohexane at 300 °C, the CA was similar to untreated P29 at 19 ± 2.9° and labeled as "P29-C300". The Ti-raw (without laser treatments) was exposed to cyclohexane-assisted low-temperature annealing of 70 °C for 2 h, resulting in a CA of 104.2 ± 8.1°, similar to untreated Ti-raw, and labeled as "Ti-raw-C70". The Ti-raw in Fig. 14 is the original Ti-6Al-4V surface before laser processing and without cyclohexane treatments. The results indicate that combining LTS with cyclohexane-assisted low-temperature annealing of 70 °C can produce a superhydrophobic surface.

Fig. 16 shows the long-term stability of superhydrophobicity on P29-C70 for 67 days. P29-C70 maintained stable superhydrophobicity for the initial 9 days. However, after this period, superhydrophobicity on P29-C70 began to degrade. Figs. 16 and 17 show that the superhydrophobicity on P29-C70 dropped to near superhydrophobicity by 26 days and gradually declined to a hydrophobicity at 67 days. P29 and P29-C300 transitioned from hydrophilicity to hydrophobicity over time. P29-C300 reached a hydrophobicity state more rapidly than P29 but experienced a decline after 6 days. The hydrophobicity of P29-C300 subsequently increased again after 12 days, reaching the maximum CA of 130.2 ± 9.9° by 67 days. P29 also exhibited a gradual increase in CA, reaching a maximum of 140.1 ± 4.7° at 67 days. P29, P29-C70, and P29-C300 were comparable at 67 days.

3.3. Discussion

3.3.1. Single ablation spot analysis

The fluence of the laser, which is the energy per unit area, plays a crucial role in determining the material's structure at the laser focus. This study measured the actual fluence to be 213.9 ± 35.3 J/cm^2. The textures shown in Fig. 2 are formed through various processes, including splashing, melting, evaporating, re-solidification, and redeposition. These processes are influenced by variations in the laser processing zone [30]. The microscale features observed are due to resolidified material accumulation, molten metal's evaporation, and recoil pressure around the laser texturing zone [43,44].

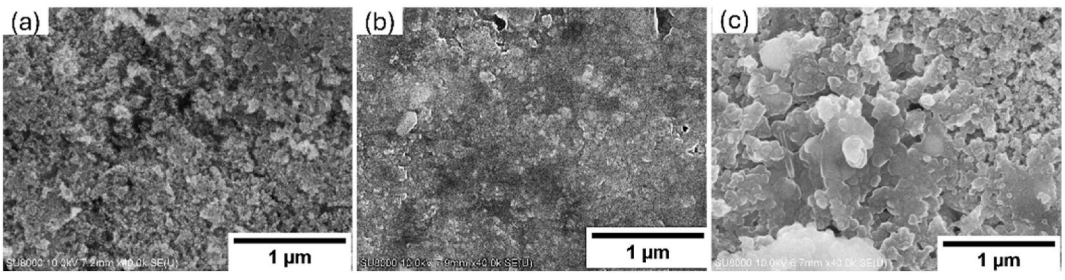

Fig. 11. FE-SEM images of laser-textured surfaces Ti-6Al-4V before and after treatment at different cyclohexane temperatures (a) P29, (b) P29-C70, and (c) P29-C300.

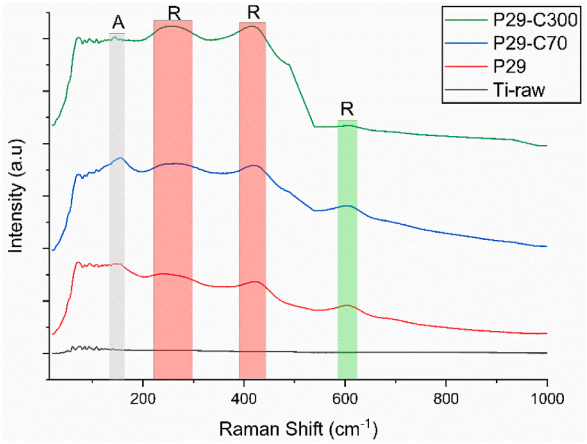

Fig. 12. Raman spectra of Ti-6Al-4V surfaces with different topographies, following treatment at various cyclohexane temperatures.

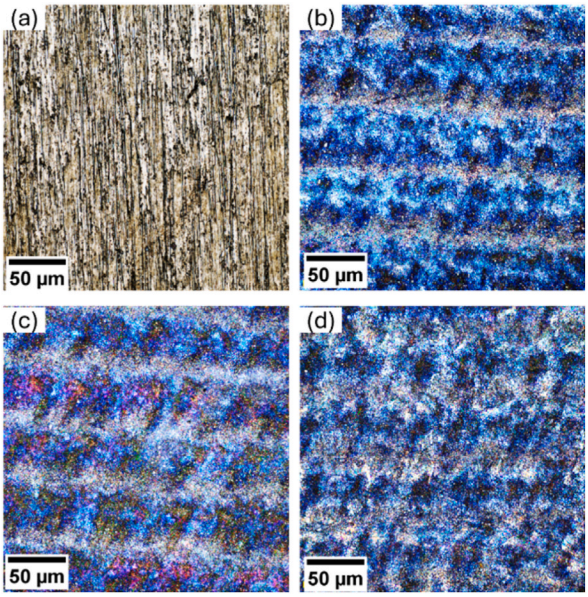

Fig. 13. CLSM images of different Ti-6Al-4V color surfaces after cyclohexane treatment: (a) Ti-raw, (b) P29, (b) P29-C70, and (c) P29-C300.

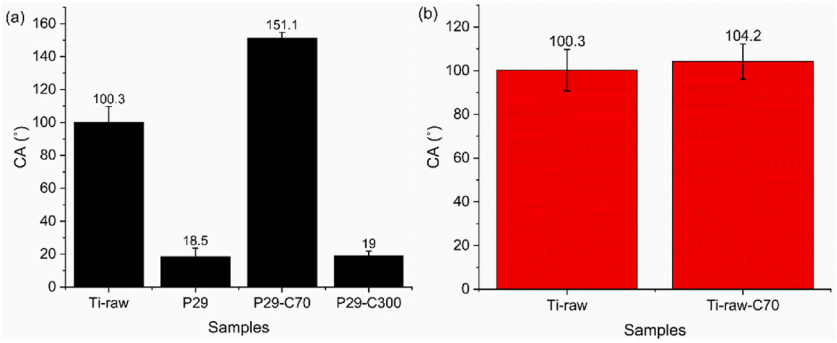

Fig. 14. Effect of cyclohexane treatment on wettability: (a) wettability measurements on LTS immediately after cyclohexane treatment; and (b) wettability comparison on Ti-raw surface before and after cyclohexane-assisted low-temperature annealing at 70 °C.

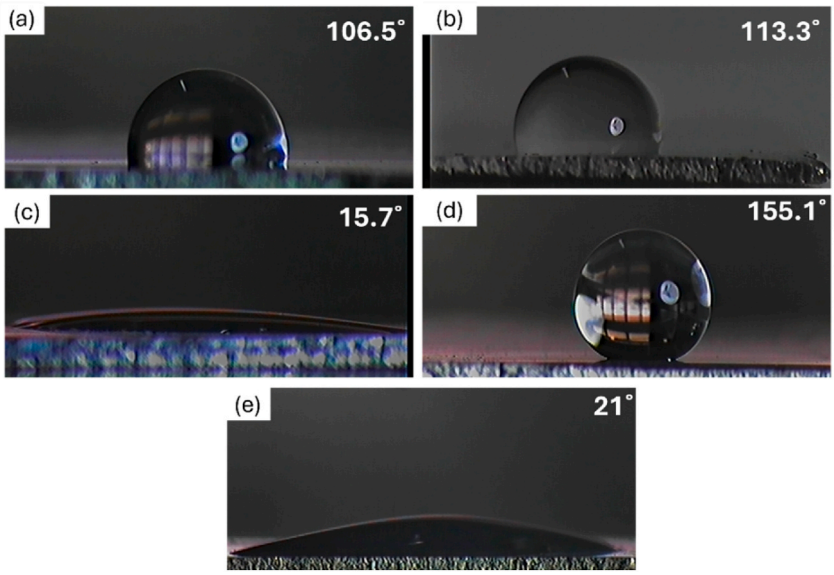

Fig. 15. Wettability on Ti-6Al-4V is taken by SANYO VCC-5755P camera: (a) Ti-raw, (b) Ti-raw-C70, (c) P29, (d) P29-C70, and (e) P29-C300.

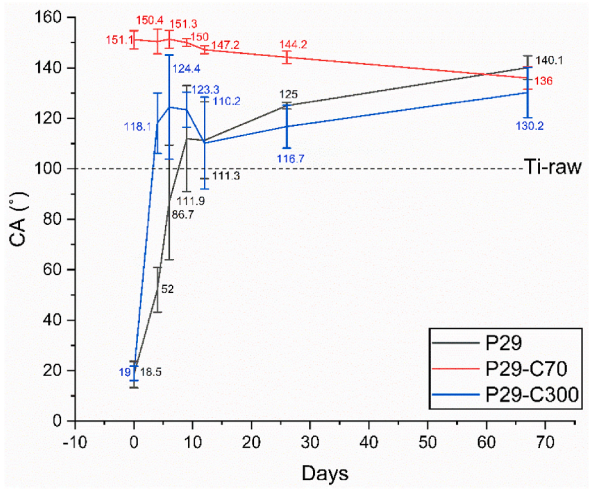

Fig. 16. The stability of water contact angle immediately after different cyclohexane treatments till 67 days.

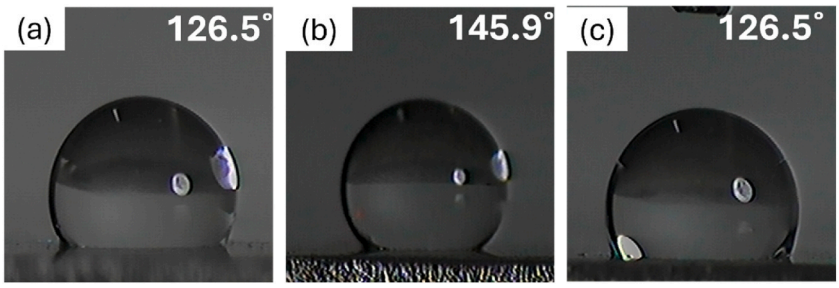

Fig. 17. Wettability on 26 days is taken by SANYO VCC-5755P camera: (a) P29, (b) P29-C70, and (c) P29-C300.

3.3.2. Surface topography and laser processing parameters

Fig. 3 reveals that different surface topographies on Ti-6Al-4V after laser processing are related to variations in pitch sizes and scanning speeds. These variations affect factors such as beam spot overlapping (BSO), pulse overlapping (PO), total incident laser energy per unit area (φ_{acc}), and the number of effective pulses per location irradiated on the Ti-6Al-4V surface, as summarized in Table 4.

Beam spot overlapping increased from 4.3 % to 45.6 % by reducing pitch sizes from 51 μm to 29 μm, then affected the decrease in V_w from 29.5 ± 4 μm to 18 ± 2.3 μm. The estimation of beam spot overlapping (BSO) in the perpendicular direction to the scanning direction can be calculated as follows [45]:

$$BSO = \left(1 - \frac{pitch}{spot\ size}\right) \times 100 \tag{1}$$

The number of effective pulses per location (N_e) and pulse overlapping affect the S_z significantly. The increase in S_z value correlated with the rise in N_e from 1.3 pulses to 3.6 pulses and pulse overlapping from 23.1 % to 71.9 %. The reduction in scanning speeds from 0.041 cms^{-1} to 0.015 cms^{-1} enhances N_e and pulse overlapping. Increased ablation depth is caused by decreased ablation threshold and improved absorption conditions brought on by heat buildup [46]. The estimation of pulse overlapping (PO) in the scanning direction and the number of effective pulses per location was conducted by Refs. [45,47]:

$$Pulse\ overlapping\ (\%) = \left(1 - \frac{speed}{repitition\ rate \times spot\ size}\right) \times 100 \tag{2}$$

$$N_e = \frac{spot\ size}{speed} \times repitition\ rate \tag{3}$$

Sample P29 exhibits greater surface roughness, as shown in Fig. 3, which is further confirmed by FE-SEM images, as shown in Fig. 4. The surface texture of Ti-6Al-4V transitions from slightly grainy to extremely coarse as pitch sizes and scanning speeds are reduced from a pitch size of 51 μm with a scanning speed of 0.041 cm/s to a pitch size of 29 μm with a scanning speed of 0.015 cm/s. The increased surface roughness in P29 is related to the slowest scanning speed of 0.015 cm/s with the smallest pitch size of 29 μm, resulting in the highest total incident laser energy per area of 108.1 J/cm^2. According to the findings, Ti-6Al-4V surface texture is influenced by beam spot and pulse overlapping, which respond to decreased pitch sizes and scanning speed. Enhanced metal surface melting is attributed to the buildup of laser pulses, whereas the spillage of the molten material is further intensified by the pressure produced by the substantial beam spot overlap. Upon reentering the surface, the droplets of significant substance and minute particles resolidified due to the motion of the laser [48,49]. The Ti-6Al-4V surfaces become rougher by reducing pitch sizes and scanning speeds due to the higher material removal and increased energy input resulting from the acceleration, deceleration, and reversal processes during the high repetition rate of scanning material processing [46]. The total incident laser energy per unit area can be mathematically represented [46]:

$$\varphi_{acc} = \frac{energy}{speed \times pitch} \tag{4}$$

3.3.3. Chemical composition of laser-textured surface

Laser processing under an ambient environment affects the surface composition of Ti-6Al-4V, as shown in Fig. 5. High-intensity laser beams cause changes in surface composition by evaporating hydrogen, oxygen, and other contaminants, leading to the formation of oxide species [50]. Heat accumulation, which comes from greater specific laser energy input with higher pulse numbers during laser processing in the ambient environment, creates various TiO_2 structures with heterogeneous peak intensities [29,51,52]. The heterogeneous distribution of TiO_2 peak intensity observed in Raman spectroscopy results can be attributed to three factors. First, particle size influences Raman intensity, with smaller particles showing lower intensity and increasing particle sizes displaying increased intensity, then declines when particle sizes are larger [53]. Second, the initial oxide layers caused the particles to adopt a core-cell configuration, shifting the Raman results depending on the shell thickness and dielectric constant [54–56]. Another factor to consider is the potential influence of nanoparticles on the molecule's Raman spectrum. Nanoparticles contribute to selective support, impacting the molecule's adsorption and orientation, resulting in diverse outcomes in the Raman spectrum [57]. A material stream with a strong focus is produced due to the laser beam's interaction with the target. The stream is commonly discharged towards the outermost layer of the target and then formed onto suitable substrates placed in front of the target. This stream consists of microscopic and highly active molecular types considered neutral or ionized within the area of interest. Nonetheless, the characteristics of deposited particles can vary based on numerous factors, including laser fluence, wavelength, pulse length, scan velocity, target

Table 4
The effect of different pitch sizes and scanning speeds on BSO, PO, N_e, and φ_{acc}.

Samples	Pitch sizes (μm)	Scanning speed (cms^{-1})	BSO (%)	PO (%)	N_e (Pulse)	φ_{acc} ($J\ cm^{-2}$)
P29	29	0.015	45.6	71.9	3.6	108.1
P34	34	0.016	36.2	70	3.3	84.4
P51	51	0.041	4.3	23.1	1.3	22.5

structure, composition of chemicals, and material temperature [58,59].

Fig. 6 shows Ti-6Al-4V phases changed after surface texturing. Anatase and rutile phases are observed after laser texturing. The Ti-6Al-4V phase compositions were affected by the high total incidence laser energy per unit area caused by decreased pitch sizes and scanning speeds. Crystal structuring with a favored growth orientation relies heavily on laser processing, making it a crucial need. High-energy laser texturing led to an increase in crystallinity, hence inducing the desired orientation. A higher magnitude of the diffraction signal indicates a larger particle size [60]. The formation of a crystalline fraction occurs within solid materials when solid materials are irradiated with slightly higher fluence. There are two sections involved in this process. The formation of the crystalline phase necessitates a significant number of laser pulses. During this initial stage, the incubation period of crystalline nuclei persists. The growth of nuclei is induced by successive pulses, leading to the development of visibly crystalline regions. This process requires a higher number of pulses to be initiated. The subsequent crystallization process occurs closer to the beam center and at higher laser fluence levels. The molten state region's outer edges can give rise to large crystalline grains as the liquefied material solidifies following the solidification of its surface [18,61]. High cooling velocities prevent the generation of nuclei [61,62]. However, peak intensities of aluminum, vanadium, and their associated phases (Al-3V, Al0.5Ti0.5V, and Ti-V) are absent in XRD results before and after laser texturing. This absence may be attributed to the complexity and non-linear nature of the Ti-6Al-4V phase transformation, which is influenced by the alloy's stoichiometry [63]. Commonly, vanadium is typically used as a β-Ti stabilizer, while aluminum acts as an α-Ti stabilizer, reducing the stability of the β-Ti phase. The concentration of these stabilizers significantly influences the dominant phase in Ti-6Al-4V alloys. The manufacturing process strongly influences the relative proportions of α-Ti and β-Ti phases, as the inherent cooling rate is critical in determining the final phase composition [64].

3.3.4. Surface color of Ti-6Al-4V after laser texturing

Fig. 3 illustrates that P51 and P29 exhibit predominantly bright areas, whereas P34 presents a combination of bright and dark areas. These color differences observed under SEM are attributable to variations in surface composition induced by laser texturing, as shown in Fig. 5. Brookite and anatase appear darker under SEM, whereas rutile particle displays a bright contrast [65]. Rutile exhibits higher brightness under SEM than anatase and brookite, attributed to its greater crystal density and smaller band gap energy relative to the other TiO_2 polymorphs [66].

Fig. 7 shows different colors on Ti-6Al-4V after laser processing. Ti-6Al-4V has different surface colors after laser processing due to different surface geometry (surface roughness), the thickness of the oxide, and the formation of optically active nanostructures during laser processing. These factors cause numerous white light scattering in Ti-6Al-4V surfaces [67]. Rajab et al. [29] explain that the Ti-6Al-4V surface exhibits a range of colors resulting from the concentrations of oxidation and nitrogen generated throughout the laser texturing process. The surface acquires a darker hue due to the rutile phase following the texturing process.

3.3.5. Effect of cyclohexane treatment on surface roughness

Figs. 10 and 11 show that the roughness of P29-C70 surfaces was smoother than that of P29 and P29-C300 surfaces. Surface roughness is decreased due to ultra-micropores filling with multiple layers of cyclohexane, which is facilitated by cyclohexane-assisted low-temperature [68]. However, cyclohexane degrades at elevated temperatures [68], resulting in P29-C300 having a surface roughness similar to that of P29. Additionally, the interaction between TiO_2 and cyclohexane at different temperatures affects the TiO_2 particle size, which results from the reaction between TiO_2 and cyclohexanol or cyclohexanone [69].

3.3.6. Chemical composition and surface color of LTS following cyclohexane treatment

Fig. 12 shows Raman spectroscopy revealed a prominent TiO_2 peak (anatase and rutile) at 605 cm^{-1} for P29-C70, while a weaker peak for P29-C300 due to the interaction between cyclohexane and TiO_2 during chemical treatment at different temperatures cyclohexane. Cyclohexane can oxidize at low temperatures [70] and with O_2 [71]. Cyclohexane can undergo oxidation, resulting in the formation of cyclohexanol (-OH), cyclohexanone (=O), and an intermediate compound known as cyclohexyl hydroperoxide [71]. Raman intensity of TiO_2 (anatase and rutile) decreases on P29-C300 because TiO_2 can be decomposed when treated at temperatures higher than 180 °C [72] or cyclohexane-covered TiO_2 during chemical treatment. Fig. 13 shows that the color changes on P29 post-treatment are related to surface roughness and different oxidation levels, as shown in Figs. 10 and 12.

3.3.7. Wettability

Fig. 8 shows that hydrophilicity increases as pitch sizes decrease. Laser processing increases the hydrophilicity of Ti-6Al-4V for several reasons, including removing organic compounds and introducing surface textures that improve surface irregularity and TiO_2 content. The exhibiting of oxide surface indicates polar abilities and often generates a hydrophilic surface on Ti-6Al-4V surfaces. Oxide features on micro/nanostructures enable rapid dispersion of water droplets, promoting their absorption by concave surface features [32,73–75]. The transition in wettability is also associated with variations in the crystalline plane orientations, which are influenced by differences in surface energies and densities [60,76,77]. Titanium dioxide is found on LTS with varying intensity levels, as mentioned in subsection *3.1.3*. The titanium dioxide on LTS exhibits hydrophilic/superhydrophilic properties due to its high surface energy and affinity for water molecules through Ti-OH [78,79]. Wenzel's theory describes the hydrophilicity changes, where increased surface roughness from laser processing alters the wetting properties from hydrophobic to hydrophilic by allowing liquids to fill surface cavities [80,81]. The equation representing the Wenzel model is as follows [81]:

$$\cos\theta_W = r\cos\theta \tag{5}$$

The equation describes the correlation of the water contact angle (CA) of the laser-textured surface (θ_W), the contact angle of the Ti-raw surface (θ), and the surface roughness factor (r). The surface roughness factor decreased as hydrophilicity increased, corresponding with a reduction in pitch sizes from 51 μm to 29 μm, as shown in Fig. 18(a). Fig. 18(b) shows that enhancing the surface roughness causes a significant change in the behavior of water on the P29 and P34 surfaces. When surface roughness increased from 0.28 μm to 0.5 ± 0.01 μm, hydrophilicity increased from 100.3 ± 9.5° to 18.5 ± 5.2°. Previously, the surface repelled water through an angle of contact measuring 100.3 ± 9.5°, but now it attracts water. The increase in hydrophilicity can be attributed to the ratio of S_z to V_w. A higher S_z/V_w ratio provides a reservoir effect that facilitates a more rapid spread of the liquid front, exceeding the spreading velocity observed on untreated surfaces [82,83]. The S_z/V_w ratio increased from 0.15 ± 0.03 to 0.36 ± 0.03 as the pitch size was reduced from 51 μm to 29 μm. Fig. 19 shows that hydrophilicity increased correspondingly with the rise in the S_z/V_w ratio.

After laser processing, hydrophilicity increased due to the offering of surface structural imperfections such as nanoscale defects. Nanoscale defects stimulate hydroxylation in LTS. The hydroxyl groups can enhance the surface hydrophilicity by generating strong bonds with water molecules on the surface rather than decreasing it [84]. Fig. 14 shows hydrophilicity of P29, which accelerates to superhydrophobicity following cyclohexane-assisted low-temperature annealing at 70 °C, as observed in P29-C70. The superhydrophobicity of P29-C70 is attributed to cyclohexane treatment at low temperatures causes cyclohexane-blocking ultra-micropores. The compound cyclohexane exhibits a robust hydrogen bonding connection when exposed to water. The ability of water to restructure itself around a nonpolar solute to sustain this association contributes to the hydrophobic impact seen [37]. Chao Wang et al. [27] compared chemical treatments using hydrophobic agents on the Ti surface with and without nanoporous structures. The hydrophobicity of Ti surfaces with nanoporous structures significantly increased compared to Ti surfaces without nanoporous structures. The wettability result was similar to that of Ruslan Melentiev et al. [85] after surface coating; the water contact angle increased due to decreased S_{dr} and S_{dq}. High adhesion is a defining characteristic of the growth of S_{dr} when liquids are distributed over it [86]. However, P29-C300 shows similar hydrophilicity with P29.

The hydrophobicity of P29 and P29-C300 increased over time due to trapped air within the valley between the recast layer and the adsorption of organic compounds from the atmosphere around it onto the oxide surface [80,87]. However, P29-C300 rose faster to hydrophobicity than P29. The superhydrophobicity of P29-C70 and the hydrophobicity of P29-C300 dropped after 6 days. The decreasing hydrophobicity of P29-C70 and P29-C300 after 6 days might be due to the degradation of the cyclohexane layer at room temperature. The melting point of cyclohexane at 6.47 °C was mentioned earlier in the introduction section, and room temperature is higher than the cyclohexane melting point. After 67 days, P29-C70 has similar hydrophobicity with P29 and P29-C300.

4. Conclusion

This study showed that the hydrophobicity of Ti-6Al-4V was tuned using a Q-switched nanosecond laser pulse at 1064 nm and cyclohexane treatments in ambient conditions. The LTS generated by a Q-switched nanosecond laser pulse at 1064 nm in this paper has several benefits, including high efficiency, high durability, and cost-effectiveness, making it suitable for large-scale production. Via experiments and analysis, the following conclusions were drawn.

(1) The surface textures and composition of Ti-6Al-4V were changed to micro/nanostructure with TiO_2 on the surface after laser processing by various pitch sizes. Different surface textures and compositions influenced different colors on the Ti-6Al-4V surface.
(2) The hydrophobicity of Ti-6Al-4V was transformed to hydrophilicity after laser processing due to Ti-6Al-4V surface transformation to micro/nanostructures with TiO_2 distribution on the surface.
(3) The hydrophilicity of LTS can be accelerated to superhydrophobicity immediately after cyclohexane-assisted annealing at 70 °C treatment for 2 h. On the other hand, Ti-raw cannot reach superhydrophobicity after being treated with low-temperature cyclohexane at 70 °C. Therefore, the superhydrophobic surface in this study can be attributed to both the structure and subsequent formation of a hydrophobic substrate.

To summarize, the superhydrophobic Ti-6Al-4V surface in this work was produced by a simple single chemical modifier combined

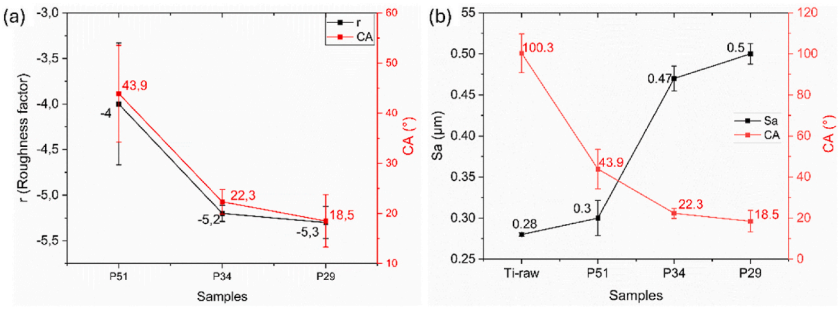

Fig. 18. Effect of different pitch sizes on surface roughness, roughness factor, and water contact angle: (a) the effect of different pitch sizes on roughness factor and water contact angle, and (b) the effect of different pitch sizes on surface roughness (S_a) and water contact angle.

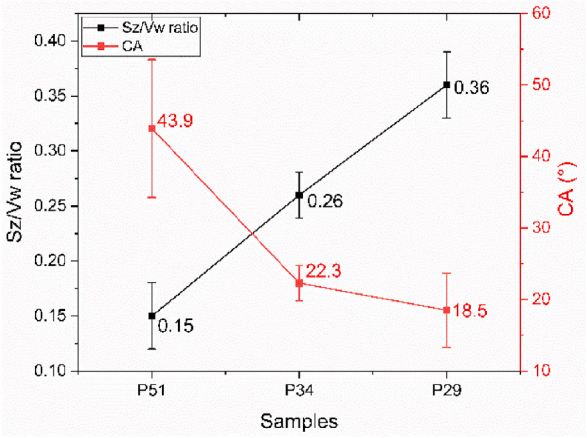

Fig. 19. Effect of different pitch sizes on S_z/V_w ratio and water contact angle.

with low heating temperature and short-duration treatment after laser texturing. An effortless and low energy-consumption method for turning hydrophilicity to superhydrophobicity on the Ti-6Al-4V surface will provide broad industrial and scientific applications.

Data availability

Data will be made available on request.

CRediT authorship contribution statement

Muhammad Budi Haryono: Writing – original draft, Methodology, Data curation, Conceptualization. **Kaung Wai Yan Lin:** Methodology. **Tanant Waritanant:** Writing – review & editing, Validation, Supervision, Methodology, Funding acquisition, Conceptualization.

Declaration of competing interest

The authors declare the following financial interests/personal relationships which may be considered as potential competing interests:

Tanant Waritanant, Ph.D reports financial support was provided by National Science Research and Innovation Fund, Thailand. If there are other authors, they declare that they have no known competing financial interests or personal relationships that could have appeared to influence the work reported in this paper.

Acknowledgements

This research project has been funded by Mahidol University (Fundamental Fund: fiscal year 2024 by National Science Research and Innovation Fund (NSRF)). Authors are thankful for instrumentation support for the XRD, Bruker, and D2 phase from the Mahidol University-Frontier Research Facility (MU-FRF) and scientists of MU-FRF, Nawapol Udpuay, Dr. Suwilai Chaveanghong, and Bancha Panyacharoen for their kind assistance.

References

[1] C.N. Elias, J.H.C. Lima, R. Valiev, M.A. Meyers, Biomedical applications of titanium and its alloys, J. Occup. Med. 60 (2008) 46–49, https://doi.org/10.1007/s11837-008-0031-1.

[2] A. Bhattacharjee, M. Khan, M. Kleiman, A.I. Hochbaum, Effects of growth surface topography on bacterial signaling in coculture biofilms, ACS Appl. Mater. Interfaces 9 (2017) 18531–18539, https://doi.org/10.1021/acsami.7b04223.

[3] S. Wu, B. Zhang, Y. Liu, X. Suo, H. Li, Influence of surface topography on bacterial adhesion: a review, Biointerphases 13 (2018) 060801, https://doi.org/10.1116/1.5054057 submitted for publication.

[4] R.Z. Valiev, I.P. Semenova, V.V. Latysh, H. Rack, T.C. Lowe, J. Petruzelka, L. Dluhos, D. Hrusak, J. Sochova, Nanostructured titanium for biomedical applications, Adv. Eng. Mater. 10 (2008) 15–17, https://doi.org/10.1002/adem.200800026.

[5] K. Gotfredsen, T. Berglundh, J. Lindhe, Bone reactions adjacent to titanium implants subjected to static load of different duration. A study in the dog (III), Clin. Oral Implants Res. 12 (2001) 552–558, https://doi.org/10.1034/j.1600-0501.2001.120602.x.

[6] F. Grizon, E. Aguado, G. Huré, M.F. Baslé, D. Chappard, Enhanced bone integration of implants with increased surface roughness: a long term study in the sheep, J. Dent. 30 (2002) 195–203, https://doi.org/10.1016/S0300-5712(02)00018-0.

[7] E. Fadeeva, V.K. Truong, M. Stiesch, B.N. Chichkov, R.J. Crawford, J. Wang, E.P. Ivanova, Bacterial retention on superhydrophobic titanium surfaces fabricated by femtosecond laser ablation, Langmuir 27 (2011) 3012–3019, https://doi.org/10.1021/la104607g.

[8] X.Q. Dou, D. Zhang, C. Feng, L. Jiang, Bioinspired hierarchical surface structures with tunable wettability for regulating bacteria adhesion, ACS Nano 9 (2015) 10664–10672, https://doi.org/10.1021/acsnano.5b04231.

[9] B.J. Privett, J. Youn, S.A. Hong, J. Lee, J. Han, J.H. Shin, M.H. Schoenfisch, Antibacterial fluorinated silica colloid superhydrophobic surfaces, Langmuir 27 (2011) 9597–9601, https://doi.org/10.1021/la201801e.

[10] K.A. Dafforn, J.A. Lewis, E.L. Johnston, Antifouling strategies: history and regulation, ecological impacts and mitigation, Mar. Pollut. Bull. 62 (2011) 453–465, https://doi.org/10.1016/j.marpolbul.2011.01.012.

[11] J. Li, G. Wang, Q. Meng, C. Ding, H. Jiang, Y. Fang, A biomimetic nano hybrid coating based on the lotus effect and its anti-biofouling behaviors, Appl. Surf. Sci. 315 (2014) 407–414, https://doi.org/10.1016/j.apsusc.2014.07.147.

[12] X. Pu, G. Li, H. Huang, Preparation, anti-biofouling and drag-reduction properties of a biomimetic shark skin surface, Biol. Open 5 (2016) 389–396, https://doi.org/10.1242/bio.016899.

[13] X. Yao, Y. Song, L. Jiang, Applications of bio-inspired special wettable surfaces, Adv. Mater. 23 (2011) 719–734, https://doi.org/10.1002/adma.201002689.

[14] J.T. Cardoso, A.G. Giron, J.M. Romano, D.H. Murillo, R. Jagdheesh, M. Walker, S.S. Dimov, J.L. Ocana, Influence of ambient conditions on the evolution of wettability properties of an IR-, ns-laser textured aluminium alloy, RSC Adv. 7 (2017) 39617–39627, https://doi.org/10.1039/c7ra07421b.

[15] J. Song, D. Wang, L. Hu, X. Huang, Y. Chen, Superhydrophobic surface fabricated by nanosecond laser and perhydropolysilazane, Appl. Surf. Sci. 455 (2018) 771–779, https://doi.org/10.1016/j.apsusc.2018.05.227.

[16] M. M. Calderon, A. Rodríguez, A. D. Ponte, M. C. M. Miñana, M. G. Aranzadi, S. M. Olaizola, Femtosecond laser fabrication of highly hydrophobic stainless steel surface with hierarchical structures fabricated by combining ordered microstructures and LIPSS, Appl. Surf. Sci. 374 (216) 81–89, doi: 10.1016/j.apsusc.2015.09.261. .

[17] A. Kurella, N.B. Dahotre, Review paper: surface modification for bioimplants: the role of laser surface engineering, J. Biomater. Appl. 20 (2005), https://doi.org/10.1177/0885328205052974.

[18] L. Hu, L. Zhang, D. Wang, X. Lin, Y. Chen, Fabrication of biomimetic superhydrophobic surface based on nanosecond laser-treated titanium alloy surface and organic polysilazane composite coating, Colloids Surfaces A Physicochem. Eng. Asp. 555 (2018) 515–524, https://doi.org/10.1016/j.colsurfa.2018.07.029.

[19] J. Li, J. Xu, Z. Lian, Z. Yu, H. Yu, Fabrication of antireflection surfaces with superhydrophobic property for titanium alloy by nanosecond laser irradiation, Opt Laser. Technol. 126 (2020) 106129, https://doi.org/10.1016/j.optlastec.2020.106129.

[20] Z. Yang, Y. Tian, Y. Zhao, C. Yang, Study on the fabrication of super-hydrophobic surface on Inconel Alloy via nanosecond laser ablation, Materials 12 (2019), https://doi.org/10.3390/ma12020278.

[21] D.V. Ta, A. Dunn, T.J. Wasley, R.W. Kay, J. Stringer, P.J. Smith, C. Connaughton, J.D. Shephard, Nanosecond laser textured superhydrophobic metallic surfaces and their chemical sensing applications, Appl. Surf. Sci. 357 (2015) 248–254, https://doi.org/10.1016/j.apsusc.2015.09.027.

[22] C. Momma, B.N. Chichkov, S. Nolte, F.V. Alvensleben, A. Tunnermann, H. Welling, B. Wellegehausen, Short-pulse laser ablation of solid targets, Opt Commun. 129 (1996) 134–142, https://doi.org/10.1016/0030-4018(96)00250-7.

[23] D.H. Murillo, A.I.A. Morales, S. Alamri, J.T. Cardoso, R. Jagdheesh, A.F. Lasagni, J.L. Ocana, Fabrication of multi-scale periodic surface structures on Ti-6Al-4V by direct laser writing and direct laser interference patterning for modified wettability applications, Opt Laser. Eng. 98 (2017) 134–142, https://doi.org/10.1016/j.optlaseng.2017.06.017.

[24] D. Patil, S. Aravindan, M.K. Wasson, P. Vivekanandan, P.V. Rao, Fast fabrication of superhydrophobic titanium alloy as antibacterial surface using nanosecond laser texturing, J. Micro Nano-Manufacturing 6 (2018), https://doi.org/10.1115/1.4038093.

[25] C.J. Yang, X.S. Mei, Y.L. Tian, D.W. Zhang, Y. Li, X.P. Liu, Modification of wettability property of titanium by laser texturing, Int. J. Adv. Manuf. Technol. 87 (2016) 1663–1670, https://doi.org/10.1007/s00170-016-8601-9.

[26] Y. Wang, X. Zhao, C. Ke, J. Yu, R. Wang, Nanosecond laser fabrication of superhydrophobic Ti6Al4V surfaces assisted with different liquids, Colloids Interface Sci. Commun. 35 (2020) 100256, https://doi.org/10.1016/j.colcom.2020.100256.

[27] C. Wang, H. Huang, Z. Zhang, L. Zhang, J. Yan, L. Ren, Formation, evolution and characterization of nanoporous structures on the Ti6Al4V surface induced by nanosecond pulse laser irradiation, Mater. Des. 223 (2022) 111243, https://doi.org/10.1016/j.matdes.2022.111243.

[28] Y. Wang, J. Chen, Y. Yang, Z. Liu, H. Wang, Z. He, Nanostructured superhydrophobic titanium-based materials: a novel preparation pathway to attain superhydrophobicity on TC4 alloy, Nanomaterials 12 (2022), https://doi.org/10.3390/nano12122086.

[29] F.H. Rajab, C.M. Liauw, P.S. Benson, L. Li, K.A. Whitehead, Production of hybrid macro/micro/nano surface structures on Ti6Al4V surfaces by picosecond laser surface texturing and their antifouling characteristics, Colloids Surf. B Biointerfaces 160 (2017) 688–696, https://doi.org/10.1016/j.colsurfb.2017.10.008.

[30] C. Guo, M. Zhang, J. Hu, Fabrication of hierarchical structures on titanium alloy surfaces by nanosecond laser for wettability modification, Opt Laser. Technol. 148 (2022) 107728, https://doi.org/10.1016/j.optlastec.2021.107728.

[31] T.P. Manoj, T.P. Rasitha, S.C. Vanithakumari, B. Anandkumar, R.P. George, J. Philip, A simple, rapid and single step method for fabricating superhydrophobic titanium surfaces with improved water bouncing and self cleaning properties, Appl. Surf. Sci. 512 (2020) 145636, https://doi.org/10.1016/j.apsusc.2020.145636.

[32] B. Zheng, G. Jiang, W. Wang, X. Mei, Fabrication of superhydrophilic or superhydrophobic self-cleaning metal surfaces using picosecond laser pulses and chemical fluorination, Radiat. Eff. Defect Solid 171 (2016) 461–473, https://doi.org/10.1080/10420150.2016.1211658.

[33] R. Bongiovanni, G. Malucelli, M. Sangermano, A. Priola, Properties of UV-curable coatings containing fluorinated acrylic structures, Prog. Org. Coating 36 (1999) 70–78, https://doi.org/10.1016/S0300-9440(99)00033-8.

[34] M.K. Bernett, W.A. Zisman, Wetting properties of tetrafluoroethylene and hexafluoropropylene copolymers, J. Phys. Chem. 64 (1960) 1292–1294, https://doi.org/10.1021/j100838a040.

[35] L. Yin, Y. Wang, J. Ding, Q. Wang, Q. Chen, Water condensation on superhydrophobic aluminum surfaces with different low-surface-energy coatings, Appl. Surf. Sci. 258 (2012) 4063–4068, https://doi.org/10.1016/j.apsusc.2011.12.100.

[36] D.A.O. Modena, A.C.G. Miranda, C. Grecco, R.E. Liebano, R.C.T. Cordeiro, R.M. Guidi, Efficacy and safety of ND:YAG 1064 nm lasers for photoepilation: a systematic review, Laser Med. Sci. 35 (2020) 797–806, https://doi.org/10.1007/s10103-019-02939-6.

[37] T.M. Raschke, M. Levitt, Detailed hydration maps of benzene and cyclohexane reveal distinct water structures, J. Phys. Chem. B 108 (2004) 13492–13500, https://doi.org/10.1021/jp049481p.

[38] Y. Ma, X. Cao, X. Feng, Y. Ma, H. Zou, Fabrication of super-hydrophobic film from PMMA with intrinsic water contact angle below 90, Polymer 48 (2007) 7455–7460, https://doi.org/10.1016/j.polymer.2007.10.038.

[39] L. Gong, W. Yang, Y. Sun, C. Zhou, F. Wu, H. Zeng, Fabricating tunable superhydrophobic surfaces enabled by surface-initiated emulsion polymerization in water, Adv. Funct. Mater. 33 (2023), https://doi.org/10.1002/adfm.202214947.

[40] Dutch Expert Committee for Occupational Standards, Cyclohexane, MAK-Collection Occup. Heal. Saf. 13 (1999), https://doi.org/10.1002/3527600418.

[41] Publich Health England, Cyclohexane General Information, Prot. Improv. Nation's Heal, 2017.

[42] C.S. Hodes, E.H. Margosches, A.P. Hutchens, M.G. Price, Toxicological review for cyclohexane, U.S. Enviromental Protection Agency 110 (2003).

[43] P. Gregorčič, B.S. Batič, M. Hočevar, Controlling the stainless steel surface wettability by nanosecond direct laser texturing at high fluences, Appl. Phys. Mater. Sci. Process 123 (2017), https://doi.org/10.1007/s00339-017-1392-5.

[44] V. Semak, A. Matsunawa, The role of recoil pressure in energy balance during laser materials processing, J. Phys. D Appl. Phys. 30 (1997) 2541–2552, https://doi.org/10.1088/0022-3727/30/18/008.

[45] J. Lehr, A.M. Kietzig, Production of homogenous micro-structures by femtosecond laser micro-machining, Opt Laser. Eng. 57 (2014) 121–129, https://doi.org/10.1016/j.optlaseng.2014.01.012.

[46] J. Schille, R. Ebert, U. Loeschner, L. Schneider, N. Welther, P. Scully, N. Goddard, H. Exner, 3D micro machining with a high repetition rate ultra short fibre laser, Fifth Int. WLT-Conference Lasers Manuf 2009 (2009).

[47] Z. Zhang, Q. Zhang, Q. Wang, Y. Fu, J. Xu, Surface microstructuring of single crystalline diamond based on the accumulated energy homogenization in the nanosecond pulsed laser ablation, Opt Laser. Technol. 138 (2021) 106839, https://doi.org/10.1016/j.optlastec.2020.106839.

[48] W. Tong, D. Xiong, Direct laser texturing technique for metal surfaces to achieve superhydrophobicity, Mater. Today Phys. 23 (2022) 100651, https://doi.org/10.1016/j.mtphys.2022.100651.

[49] Z. Li, G. Xue, Y. Wu, X. Wang, H. Pan, Preparation of superhydrophobic surfaces based on rod-shaped micro-structure induced by nanosecond laser, Crystals 11 (2021), https://doi.org/10.3390/cryst11111274.
[50] V. Romano, L. Torrisi, M. Cutroneo, V. Havranek, G. D'Angelo, Raman investigation of laser-induced structural defects of graphite oxide films, EPJ Web Conf. 167 (2018) 2–6, https://doi.org/10.1051/epjconf/201816704011.
[51] A.P.D. Pino, P. Serra, J.L. Morenza, Coloring of titanium by pulsed laser processing in air, Thin Solid Films 415 (2002) 201–205, https://doi.org/10.1016/S0040-6090(02)00632-6.
[52] E. György, A.P. D Pino, P. Serra, J.L. Morenza, Structure formation on titanium during oxidation induced by cumulative pulsed Nd:YAG laser irradiation, Appl. Phys. Mater. Sci. Process 78 (2004) 765–770, https://doi.org/10.1007/s00339-002-2054-8.
[53] D.A. Gómez, J. Coello, S. Maspoch, The influence of particle size on the intensity and reproducibility of Raman spectra of compacted samples, Vib. Spectrosc. 100 (2019) 48–56, https://doi.org/10.1016/j.vibspec.2018.10.011.
[54] M.M. Miranda, C. Gellini, E. Giorgetti, Surface-enhanced Raman scattering from copper nanoparticles obtained by laser ablation, J. Phys. Chem. C 115 (2011) 5021–5027, https://doi.org/10.1021/jp1086027.
[55] R.M. Tilaki, A.I. Zad, S.M. Mahdavi, Size, composition and optical properties of copper nanoparticles prepared by laser ablation in liquids, Appl. Phys. Mater. Sci. Process 88 (2007) 415–419, https://doi.org/10.1007/s00339-007-4000-2.
[56] T. Tsuji, K. Iryo, Y. Nishimura, M. Tsuji, Preparation of metal colloids by a laser ablation technique in solution: influence of laser wavelength on the ablation efficiency (II), J. Photochem. Photobiol. Chem. 145 (2001) 201–207, https://doi.org/10.1016/S1010-6030(01)00583-4.
[57] M. Guo, Y. Zhao, C. Feng, S. Li, Y. Jiang, Surface and shape unification of excimer pulse irradiated Ag nanoparticles and associated surface-enhanced Raman scattering properties, J. Laser Appl. 29 (2017), https://doi.org/10.2351/1.4979093.
[58] F. Neri, S. Trusso, C. Vasi, F. Barreca, P. Valisa, Raman microscopy study of pulsed laser ablation deposited silicon carbide films, Thin Solid Films 332 (1998) 290–294, https://doi.org/10.1016/S0040-6090(98)00994-8.
[59] C. Byram, S.S.B. Moram, V.R. Soma, Surface-enhanced Raman scattering studies of gold-coated ripple-like nanostructures on iron substrate achieved by femtosecond laser irradiation in water, J. Raman Spectrosc. 50 (2019) 1103–1113, https://doi.org/10.1002/jrs.5617.
[60] J. Li, S. Zhao, F. Du, Y. Zhou, H. Yu, One-step fabrication of superhydrophobic surfaces with different adhesion via laser processing, J. Alloys Compd. 739 (2018) 489–498, https://doi.org/10.1016/j.jallcom.2017.12.252.
[61] T. Kunkel, Y. Vorobyov, M. Smayev, P. Lazarenko, V. Veretennikov, V. Sigaev, S. Kozyukhin, Experimental observation of two-stage crystallization of Ge2Sb2Te5 amorphous thin films under the influence of a pulsed laser, J. Alloys Compd. 851 (2021) 156924, https://doi.org/10.1016/j.jallcom.2020.156924.
[62] S.J. Li, L.P. Kong, Y.C. Liu, Y.Z. Huang, K. Chen, Y.C. Li, J.H. Qiao, H.T. Liu, Y. Luo, X.W. Li, D.K. Zhang, UV laser-ablated Cu superwetting surface with improved anti-icing and antibacterial properties, Colloids Surfaces A Physicochem. Eng. Asp. 639 (2022) 128282, https://doi.org/10.1016/j.colsurfa.2022.128282.
[63] S.M.Q.M. Ramli, N.A. Fadil, H. Yahya, W.F.F.W. Ali, Structural and thermal characteristics of Ti6Al4V (Ti64) metal powders for direct energy deposition, Mater. Today Proc. 66 (2022) 2919–2923, https://doi.org/10.1016/j.matpr.2022.06.558.
[64] L. Bolzoni, F. Yang, X-ray diffraction for phase identification in Ti-based alloys: benefits and limitations, Phys. Scripta 99 (2024) 1–11, https://doi.org/10.1088/1402-4896/ad4785.
[65] J. Li, H. Yang, Q. Li, D. Xu, Enlarging the application of potassium titanate nanowires as titanium source for preparation of TiO2 nanostructures with tunable phases, CrystEngComm 14 (2012) 3019–3026, https://doi.org/10.1039/C2CE06672F.
[66] S.D. Mo, W.Y. Ching, Electronic and optical properties ofthree phases oftitanium dioxide: rutile, anatase, and brookite, Phys. Rev. B 51 (1995) 23–32, https://doi.org/10.1103/PhysRevB.51.13023.
[67] K. Ronoh, J. Novotný, L. Mrňa, A. Knápek, D. Sobola, Surface structuring of the CP titanium by ultrafast laser pulses, Appl. Sci. 14 (2024) 3164, https://doi.org/10.3390/app14083164.
[68] R.S. Mikhail, S. Need, A. M Khalil, Heat of immersion of pure and doped magnesia in cyclohexane, Discuss. Faraday Soc. 52 (1971) 187–195, https://doi.org/10.1039/DF9715200187.
[69] J.T. Carneiro, A.R. Almeida, J.A. Moulijn, G. Mul, Cyclohexane selective photocatalytic oxidation by anatase TiO2: influence of particle size and crystallinity, Phys. Chem. Chem. Phys. 12 (2010) 2744–2750, https://doi.org/10.1039/b919886e.
[70] R. Antony, S.T.D. Manickam, S. Balakumar, Cu(II), Co(II) and Ni(II) complexes installed on functionalized silica surface for hydrogen peroxide assisted cyclohexane oxidation, J. Inorg. Organomet. Polym. Mater. 27 (2017) 418–426, https://doi.org/10.1007/s10904-016-0482-8.
[71] J. Hao, H. Cheng, H. Wang, S. Cai, F. Zhao, Oxidation of cyclohexane-A significant impact of stainless steel reactor wall, J. Mol. Catal. Chem. 271 (2007) 42–45, https://doi.org/10.1016/j.molcata.2007.02.031.
[72] Y. Mizuno, F.K. King, Y. Yamauchi, T. Homma, A. Tanaka, Y. Takakuwa, T. Momose, Temperature dependence of oxide decomposition on titanium surfaces in ultrahigh vacuum, J. Vac. Sci. Technol. A Vacuum, Surfaces, Film. 20 (2002) 1716–1721, https://doi.org/10.1116/1.1500746.
[73] A. Samanta, Q. Wang, S.K. Shaw, H. Ding, Roles of chemistry modification for laser textured metal alloys to achieve extreme surface wetting behaviors, Mater. Des. 192 (2020) 108744, https://doi.org/10.1016/j.matdes.2020.108744.
[74] J. Bico, U. Thiele, D. Quéré, Wetting of textured surfaces, Colloids Surfaces A Physicochem. Eng. Asp. 206 (2002) 41–46, https://doi.org/10.1016/S0927-7757(02)00061-4.
[75] G. Azimi, R. Dhiman, H.M. Kwon, A.T. Paxson, K.K. Varanasi, Hydrophobicity of rare-earth oxide ceramics, Nat. Mater. 12 (2013) 315–320, https://doi.org/10.1038/nmat3545.
[76] A.W. Neumann, R.J. Good, Thermodynamics of contact angles. I. Heterogeneous solid surfaces, J. Colloid Interface Sci. 38 (1972) 341–358, https://doi.org/10.1016/0021-9797(72)90251-2.
[77] C.G.J. Prakash, R. Prasanth, Approaches to design a surface with tunable wettability: a review on surface properties, J. Mater. Sci. 56 (2021) 108–135, https://doi.org/10.1007/s10853-020-05116-1.
[78] B.J. Li, H. Li, L.J. Huang, N.F. Ren, X. Kong, Femtosecond pulsed laser textured titanium surfaces with stable superhydrophilicity and superhydrophobicity, Appl. Surf. Sci. 389 (2016) 585–593, https://doi.org/10.1016/j.apsusc.2016.07.137.
[79] J. Liang, K. Liu, D. Wang, H. Li, P. Li, S. Li, S. Su, S. Xu, Y. Luo, Facile fabrication of superhydrophilic/superhydrophobic surface on titanium substrate by single-step anodization and fluorination, Appl. Surf. Sci. 338 (2015) 126–136, https://doi.org/10.1016/j.apsusc.2015.02.117.
[80] J. Long, M. Zhong, H. Zhang, P. Fan, Superhydrophilicity to superhydrophobicity transition of picosecond laser microstructured aluminum in ambient air, J. Colloid Interface Sci. 441 (2015) 1–9, https://doi.org/10.1016/j.jcis.2014.11.015.
[81] R.N. Wenzel, Resistance of solid surface to wetting by water, Ind. Eng. Chem. 28 (1936) 988–994, https://doi.org/10.1017/cbo9781316146743.
[82] D. Quéré, Rough ideas on wetting, Phys. A Stat. Mech. its Appl. 313 (2002) 32–46, https://doi.org/10.1016/S0378-4371(02)01033-6.
[83] G. McHale, N.J. Shirtcliffe, S. Aqil, C.C. Perry, M.I. Newton, Topography driven spreading, Phys. Rev. Lett. 93 (2004) 1–4, https://doi.org/10.1103/PhysRevLett.93.036102.
[84] X. Li, Y. Jiang, Z. Jiang, Y. Li, C. Wen, J. Lian, Reversible wettability transition between superhydrophilicity and superhydrophobicity through alternate heating-reheating cycle on laser-ablated brass surface, Appl. Surf. Sci. 492 (2019) 349–361, https://doi.org/10.1016/j.apsusc.2019.06.145.
[85] R. Melentiev, F. Fang, S.K.R. Narala, Influence of different pretreatments on Ti-6Al-4V surface integrity and scratch-resistance of epoxy coating: analysis of topography, microstructure, chemistry and wettability, Surf. Coating. Technol. 404 (2020) 126436, https://doi.org/10.1016/j.surfcoat.2020.126436.
[86] F. Blateyron, The areal feature parameters, in: R. Leach (Ed.), Characterisation of Areal Surface Texture, Springer Berlin Heidelberg, Berlin, Heidelberg, 2013, pp. 45–65, https://doi.org/10.1007/978-3-642-36458-7_3.
[87] S. Khorsand, K. Raeissi, F. Ashrafizadeh, M.A. Arenas, A. Conde, Corrosion behaviour of super-hydrophobic electrodeposited nickel-cobalt alloy film, Appl. Surf. Sci. 364 (2016) 349–357, https://doi.org/10.1016/j.apsusc.2015.12.122.